

Variability of the Sodium D-line ratio in the Nightglow

Karoline N

19. December 2012

Contents

1	Introduction	1
2	Theory	1
2.1	The MLT	1
2.2	Sodium Chemistry in the MLT	3
2.3	OH Chemistry in the MLT	6
2.4	Gravity Waves	7
2.5	Mathematical Modelling of Gravity Waves	10
2.6	Filters	13
3	Method	17
3.1	Imaging System	17
3.1.1	CCD Camera	17
3.1.2	Camera Control	17
3.1.3	Optics of the Imaging System	17
3.2	The Filter Wheel	21
4	Results	22
4.1	December 1st	22
4.2	December 3rd	27
5	Discussion	35
5.1	Results	35
5.2	Problems Encountered in the Course of the Project	36
6	Conclusion	36

1 Introduction

The sodium airglow is caused by reactions between ablated interplanetary dust and atmospheric oxygen at 90 km. These reactions give rise to a 5 km thick luminescent layer. Sodium emits light at two discrete frequencies at 590 nm. This is often referred to as the sodium doublet. For more than 80 years, the sodium doublet has been used to remotely sense atmospheric dynamics, chemical processes, and general circulation as well as their role in regulating the climate and knowledge of the fundamental chemistry that takes place in this region is essential. However, recent discoveries suggest that there is a variation in the intensity ratio between the two lines in the doublet, suggesting that not all is fully understood about the chemistry in this region. Laboratory experiments show a strong dependence on the O/O₂ ratio through quenching of its source molecule O₂. (ProposalFRINATEK2011)

It is thought that atmospheric gravity waves perturb the chemistry in this region. Gravity waves in the atmosphere are mechanical waves created in a number of ways, including airflow over mountains and convective activity in the atmosphere. These waves may propagate upwards into the the stratosphere and mesosphere from lower regions in the atmosphere, their amplitudes increasing as the atmospheric density decreases. Particularly in the mesosphere these amplitudes can grow quite large and the waves can exert considerable influence on the mean atmospheric state there. (Andrews, David G., An Introduction to ATMOSPHERIC PHYSICS, Second Edition, Cambridge, pages 12-13)

The focus of this project is on the observation of the sodium doublet in the images of the night time sky over Trondheim. The hope is that is is possible to observe the way the ratio between the to lines in the sodium spectre varies when the relative concentrations of the airglow producing species is disrupted by the gravity waves. This should be done using a narrow-band filter sufficiently narrow to be able to distinguish between the two frequencies, a telecentric lens system and an astronomical type camera with a CCD detector. Gravity waves are thought to play an important role in long-term climate effects. Airglow measurement is but one method of studying gravity waves. Other methods include ground-based radars, lidar measurement, rockets and air-balloons.

2 Theory

The theoretical foundations for this paper is the sodium and hydroxyl chemistry in the MLT and the way sodium emits radiation under the conditions there and the manner in which gravity waves affect these processes.

2.1 The MLT

The different layers in the atmosphere are defined by the temperature profile of the atmosphere. The region of interest for this paper is the MLT (mesosphere/lower thermosphere). It stretches from about 75 to 110 km in the atmosphere. It is often used as

the boundary region between the atmosphere and space. It is a chaotic place, subject to high-energy solar electro-magnetic radiation and solar winds from above, while wave motion in the form of gravity waves, tidal waves and planetary waves deposit momentum into the MLT from below.

The mesosphere begins at the stratopause, at a height of 50 km. In the mesosphere, the temperature decreases with height from a local temperature maxima in the stratopause to a temperature minima in the mesopause. The mesopause is located at about 85 to 100 km, depending on the season. In the thermosphere, located just above the mesopause, the temperature begins to rise with height, caused by the absorption of X-rays and high-energy UV-radiation. Here, temperatures can reach as much as 1000 K, although temperature is nothing but a kinetic concept at this height, since density and pressure is very low. The low temperature in the mesosphere is due to the fact that most of the solar EUV (extreme ultra-violet), radiation with wavelengths below 120 nm, is absorbed in the thermosphere, while at the same time the pressure in the mesosphere is too low for any significant amount of O₃ formation through O and O₂ recombination. Furthermore, due to the low pressure of the mesosphere, CO₂ acts as a infrared radiator, contributing directly to the cooling.

The MLT is also coldest in summer, as opposed to the lower parts of the atmosphere which are coldest in winter. The gravity waves, which originate in the troposphere from several causes such as orographic forcing, cumulo-nimbus storms, and cyclonic fronts, propagate upwards, their amplitudes increasing with falling pressure. Much momentum is lost in the stratosphere, but waves with the shorter periods reach the upper mesosphere. The low pressure here leads to a collapse of the wave and momentum, and energy is deposited into the MLT. This extra energy leads to a drag on the zonal winds, resulting in a southward meridional flow (for summer in the northern hemisphere). The upwelling air at high latitudes which feeds this flow is cooled by adiabatic expansion. Temperatures may fall below 120 K; if this region were in thermal equilibrium the temperature would be 220 K. Air from the entire global mesosphere is sucked into the lower stratosphere via the Antarctic polar vortex.

The very low pressure in the MLT region has several consequences. For one, it means that the mean free path of the air molecules is very large - at 110 km it approaches 1 m. Bulk motion cannot be sustained and diffusion dominates. As for the chemistry, atomic oxygen is the most important reactive species in the MLT. Atomic oxygen is depleted from the MLT at the rate of O₃ forming from the combination of O and O₂. For low pressures, this reaction is pressure dependent. At above 82 km, the time constant for oxygen removal exceeds 12 hours, meaning that an active radical chemistry lives through the night.

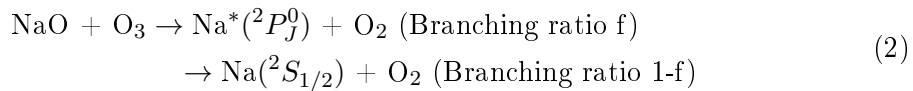
Ablated interplanetary dust is the source of the sodium in the MLT. [?] There are two ways for this dust to enter the atmosphere; either from meteor showers that

are the remnants of a comet, such as the Perseids and Leonids, or as members of the Mars-Jupiter asteroid belt. Earth is continuously peppered with this dust. Most burn up in the atmosphere, leaving behind trails of elements that would not else be found in the atmosphere.

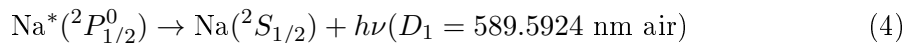
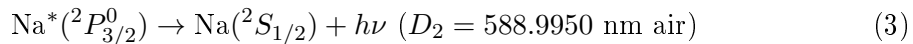
2.2 Sodium Chemistry in the MLT

The airglow is a faint, continuous glow between 40 and 400 km. It is observable from all latitudes. It contains atomic and molecular emission lines, bands and continua. The reactions responsible for this glow are chemi-luminescent. Relative large concentrations of atomic oxygen is responsible for most of these reactions that take place at heights above 80 km, either directly or indirectly. The Na layer generally peaks at around 90 km, with a FWHM of about 5 km. [Clemesha et.al.]

Radiation in the nightglow was first observed in 1929 [Slipher, 1929]. In 1938, Bernard discovered that the radiation was due to the $\text{Na}(3^2P_J - 3^2S_{1/2})$. In the year after, Chapman proposed the following set of equations to explain the radiation:



The excited sodium atom emits radiation at two discrete frequencies



The reactions 1 and 2 are known as the Chapman reactions. Initially, the problem of validating the Chapman reactions were twofold; that they had to be very fast reactions and the size of the branching ratio.

[Slanger 2005] Laboratory experiments have shown that that reactions 1 and 2 are indeed fast enough to generate the observed D-line intensity of 30 - 150 R. The reaction rate of 1 is the dominant rate, since at above 84 km the concentration of ozone is much smaller than the concentration of atomic oxygen [Plane 2003].

Several studies have been carried out to estimate the branching ratio f . [Clemesha, 1995] estimated the ratio to lie between 0.05-0.2. This experiment was carried out in northern Brazil; a rocket measured the D-line emission profile, while a ground-based lidar preformed Na concentration measurements. [Hecht et.al, 2000] did a similar rocket/lidar

experiment in Puerto Rico which produced a lower branching ratio, finding $f=0.02-0.04$. In one way did this experiment differ from the [Clemesha, 1995]; the mesopause was unusually cold that night(165 K) and the Na layer peaked at 95 km.

These results are both quite larger than the early laboratory experiments [Plane and Husain, 1986] which put the branching ratio to be less than 0.01. To resolve this apparent disagreement, a series of laboratory experiments were carried out. [Shi et.al, 1993; Wright et.al, 1993] showed that 1 produces NaO almost entirely in the low lying NaO($A^2\sigma^+$) excited electronic state rather than the π^2 state. The A state has a long radiative lifetime and it is not significantly quenched in this time, so that most reactions in the mesosphere the 2 it is the NaO(A) rather than NaO(X) that is involved [Joo et.al 1999]. Secondly, [Griffin et.al 2001] showed experimentally that for the NaO(A) + O reaction, $f = 0.14 \pm 0.04$. This experiment has reconciled the field observations with the chemistry, and that the previous studies with the low value f probably involved the NaO(X) state.

The ratio between the D_2 and the D_1 , sometimes referred to as R_D in this paper, was long taken to be 2.0 if the $J = 3/2$ and $J = 1/2$ spin orbit levels of the Na($^2P_J^0$) were produced according to their statistical weights in quantum mechanics. Furthermore, the Fabry-Perot measurements of Sipler and Biondi in 1978 showed this ratio to be 1.98 ± 0.1 . Since then, the ratio was for more than 30 years taken to be 2.0.

It was long believed that the Na chemistry of the upper atmosphere was well understood, and this ratio has therefore long been used as a tracer for atmospheric motion, either by measuring the wave structure in the Na airglow or by using resonance-fluorescence lidar observations of the D-lines to measure variations in the Na abundance and its temperature.

In 2005, Slanger et. al. discovered that this ratio D_2/D_1 varies in fact between ~ 1.2 to ~ 1.8 . The data suggested a semiannual oscillation (SAO) in the ratio with maxima at the equinoxes and minima at the solstices, see figure 1. This is a easily observed effect, with a very large high-to-low amplitude.

[Slanger et.al.] It would seem that the Chapman reactions are independent of temperature. This is not a given, reactions 2 could be temperature dependent. No field studies have been able to show a consistent dependence on temperature, while laboratory studies have shown this ratio to be independent of temperature. However, much point to a high sensitivity with regards to the $[O]/[O_2]$ ratio. Slanger et. al. [2005] postulated that the variable ratio is due to O reacting with NaO($A^3\Sigma^+$), produced from the reaction between Na and O_3 , in competition with a quenching of O_2 to produce NaO($X^2\Pi$). The first reaction would give a D_2/D_1 ratio greater than 2.0, whereas the second reaction is responsible for producing a D_2/D_1 ratio at about 1.3.

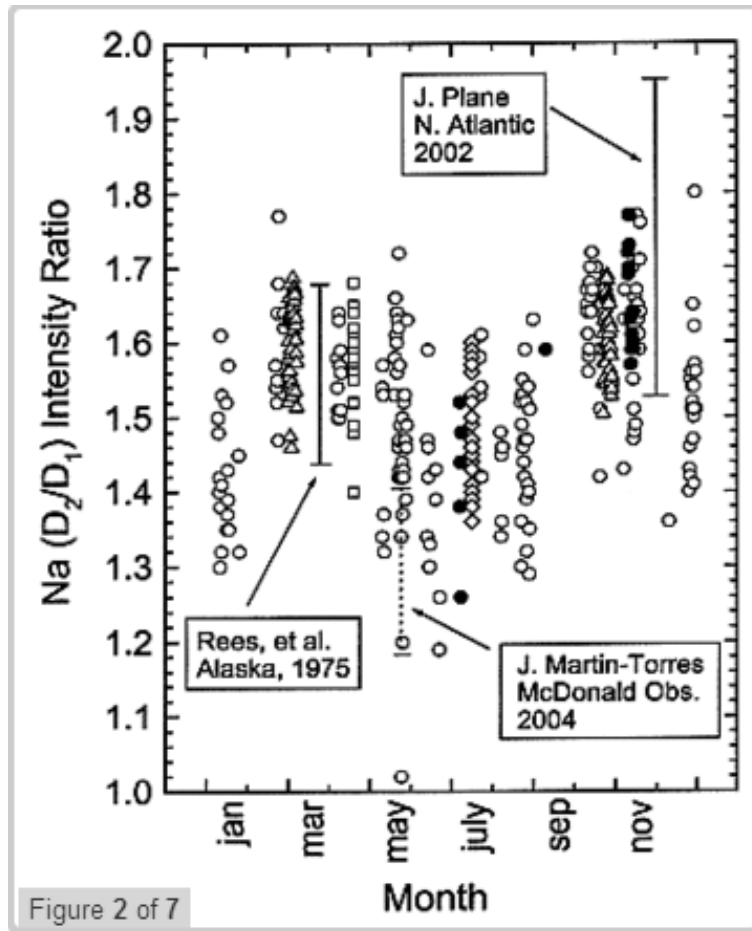
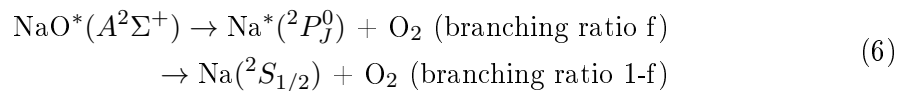
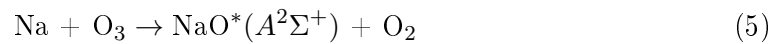
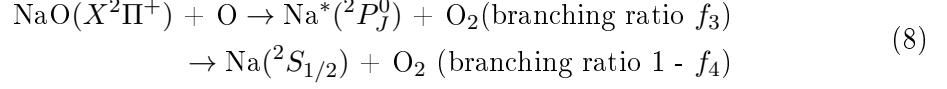
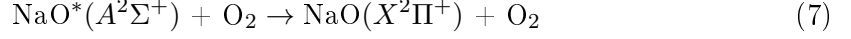


Figure 1: D-line variability over the year

Slanger et. al.[2005] proposed a solution to this conundrum; a modification to the Chapman reactions 1 and 2 based on the quenching of an intermediate excited state $\text{NaO}^*(A^2\Sigma^+)$ by molecular oxygen. Its ground state $\text{NaO}(X^2\Pi^+)$ could then react with atomic oxygen and from $\text{Na}^*(^2P_j^0)$ with populations different from their quantum mechanical statistical weights. This would lead to a lower D-line ratio. Slanger et. al. [2005] suggested the following modification to the Chapman mechanism.





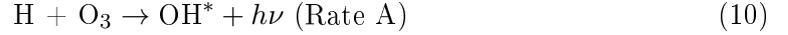
Reactions 6 and 8 would produce $\text{Na}^*(^2P_j^0)$ with different D-line ratios. f_2 and f_4 will most likely also be different. The D-line ratio observed in the atmosphere will then be a weighed sum of the two reactions, which in turn will be proportional to the O/O_2 ratio in the Na emission region.

2.3 OH Chemistry in the MLT

Sodium can react with oxygen in the MLT to create airglow; as can hydrogen. The hydroxyl layer peaks around 87 km with a FWHM of 5-8 km. The production of the excited hydroxyl state are due to the following set of equations.



Equations 10 and 11 describe the loss of hydroxyl:



In 11, M can be O, O_2 or N_2 . At steady-state production equals loss:

$$k_h[\text{H}][\text{O}_3] = A[\text{OH}^*] + K_q[\text{M}][\text{OH}^*] \quad (12)$$

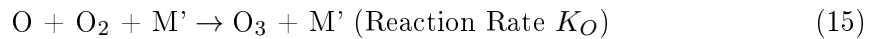
where $[]$ symbolises mean concentration.

$$I_j = [\text{OH}^*]A_j \quad (13)$$

Rewriting equation 12 to give concentration of excited stated hydroxyl results in the following equation.

$$[\text{OH}^*] = \frac{k_H[\text{H}][\text{O}_3]}{A + K_q[\text{M}]} \quad (14)$$

Furthermore, the production and loss of night-time ozone adhere to the following set of chemical equations.





Loss and production of ozone must equal for ozone.

$$K_O[\text{O}][\text{O}_2][\text{M}'] = k_H[\text{H}][\text{O}_3] \quad (17)$$

In 17, M' is a unspecified third body. Solving 17 for [O₃] gives:

$$[\text{O}_3] = \frac{K_O[\text{O}_2][\text{O}][\text{M}']}{k_H[\text{H}]} \quad (18)$$

Substituting the result for [O₃] into 14 gives:

$$[\text{OH}^*] = \frac{K_O[\text{O}][\text{O}_2][\text{M}']}{A + K_q[\text{M}]} \quad (19)$$

Thus, as the intensity of a hydroxyl band is given by 13, it becomes obvious that the intensity of a hydroxyl band emission is directly proportional to the [O][O₂] product. In other words, the O/O₂ ratio is the direct cause of the OH intensity. A high O/O₂ ratio leads to a high concentration of hydroxyl. A high O/O₂ ratio also leads to a high D₂/D₁ ratio. Consequently, can be used as an indirect measure of the O/O₂ ratio. In this project, hydroxyl airglow spectroscopy is used for locating periods of high/low O/O₂ ratios for the study of the sodium airglow images at these times of night.

2.4 Gravity Waves

Gravity waves is a type of mechanical waves that may arise in several media where gravity works as the restoring force. Generally speaking, gravity waves may occur in any media where the density decreases with height or in the interface between two media with different density, although these are known as surface waves found for instance on the ocean surface, as opposed to the internal gravity waves found in the atmosphere. Sometimes referred to as buoyancy waves, they depend on buoyancy in order to exist; the key principle is that denser material rise above less dense material and is then restored by gravity.

The waves may be generated in a number of ways. One such way is air flowing over a mountain range. As the waves propagate vertically, their amplitude grows due to energy conservation per unit volume. As the waves get higher up in the atmosphere, the neutral density decreases and in order to conserve its kinetic energy.

In order to visualise this process, it pays to imagine a corrugated sheet moving through a fluid at velocity c . The movement causes air to oscillate and a wave to propagate away.

As can be seen in figure, at point A the corrugations will be moving forward, forcing the air upwards and forwards, following the purple line in the figure. Thus, air will be compressed, leading to an increase in pressure along this line and making the entire grey area a region of high pressure. At B, it will appear as if the corrugation is moving away.

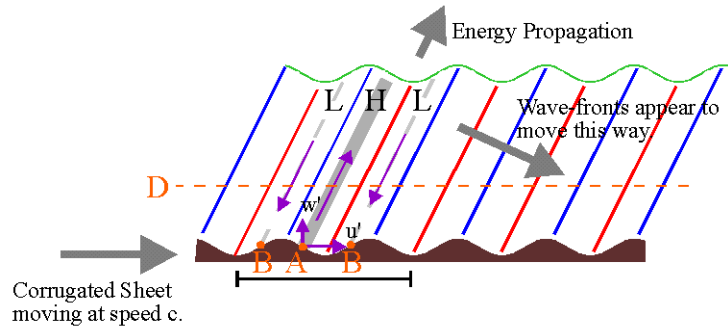


Figure 2: Corrugated sheet moving through air

Hence, air in this region will fall, and the broken grey lines will be a region of low pressure.

Vertical displacements will follow the corrugations. The upward displacement of the air parcels will be greatest along the blue lines. Adiabatic cooling will cool these air parcels as they rise. On the red lines, the downward displacement will be the greatest. Since the air parcels are sinking here, they will experience adiabatic heating and they will be the hottest parts of the wave.

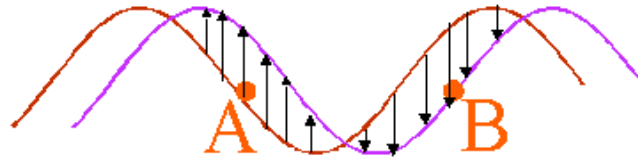


Figure 3: Movement of points A and B

The wavefronts move with the corrugations, and so to an observer they will appear to follow the grey arrow sloping down and to the right, moving with the phase velocity of the wave. The energy propagation will move up to the right, as was the air in point A. This is the reason for the waves being able to carry energy up in the atmosphere.

From reference system of the corrugated sheets however, the picture looks different. From this point of view, the whole system will appear stationary.

Then there is also the question of the stability of the atmosphere to consider. At the top of the oscillation, the air is cooler than the surrounding air; the mark of a stable atmosphere. At the bottom of the oscillation, the air parcel will be warmer than its surroundings and it will rise again. Consequently, gravity waves require a stable atmosphere.

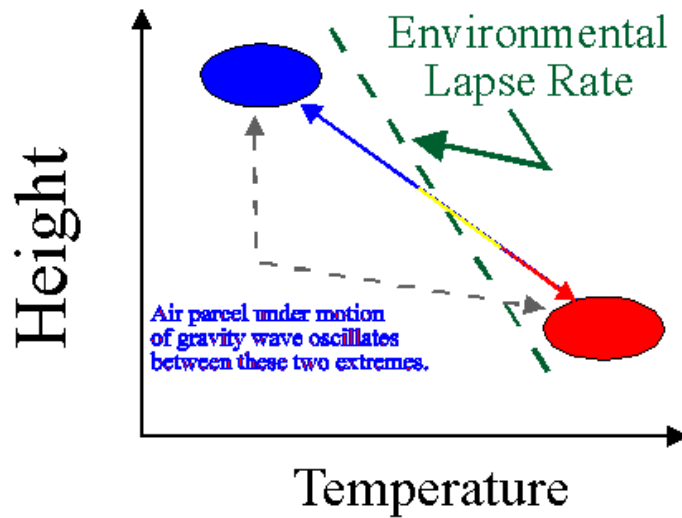


Figure 4: Adiabatic lapse rate

If gravity waves are generated in a stable part of the atmosphere and it propagates upward, it may come to encounter an unstable region of the atmosphere. The waves will not be able to pass this region and will bounce back, depositing much of the energy. Likewise, should the waves encounter a region in which the wind speeds of the background exceed the phase velocity of the gravity waves, further upward propagation will be impossible. The result is popularly referred to as a "sonic boom"; the amplitude grows very large due to the wave moving along with the air. Eventually, the wave breaks down and destroys itself, dumping momentum and energy into the surrounding atmosphere.

For better understanding these motions, the Brunt-Vaisala frequency is introduced.

$$\tau_B = \frac{2\pi}{\sqrt{\frac{g}{T}(\Gamma_a - \Gamma_e)}} \quad (20)$$

T is mean temperature, Γ_a is the adiabatic lapse rate and Γ_e is the environmental lapse rate. This period corresponds to the period if an air parcel is displaced and allowed to oscillate freely. The Brunt-Vaisala frequency can be used to relate the horizontal and vertical wavelength of the gravity waves. The intrinsic horizontal phase speed is $c_{int} = \frac{\lambda}{T}$, where λ is the wavelength and T is the period.

The horizontal wavelength is by definition the horizontal distance between identical wave-fronts. Similarly, the vertical wavelength is the vertical distance between identical wave-fronts. Generally speaking, horizontal wavelengths are much longer than the vertical ones; vertical wavelengths being on the order of a few hundred metres to a few tens of

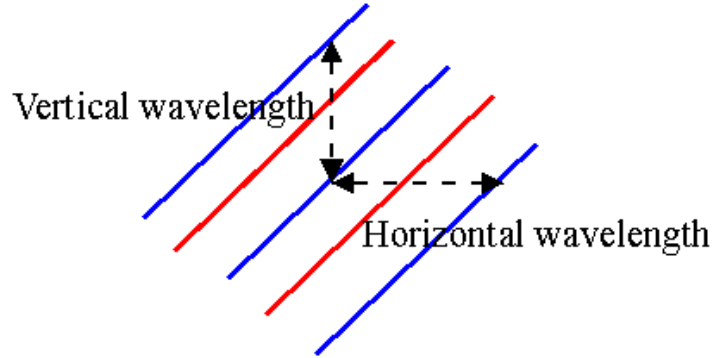


Figure 5: Horizontal and vertical wavelength

kilometres while the horizontal wavelengths can be as long as hundreds and thousands of kilometres. As promised above, the following equation relates the horizontal and vertical wavelengths:

$$\frac{\lambda_H}{\lambda_V} = T \quad (21)$$

Here, λ_H is the horizontal wavelength and λ_V is the vertical wavelength. It is worth noting that equation 21 is invalid for very short or very long periods.

For observing gravity waves in the MLT, this project focuses on taking pictures of the airglow with an all-sky CCD camera with a suitable filter in place. The resulting image is a picture of the airglow intensity across the sky. Variations are due to vertical displacement of air parcels by the gravity waves. The air here is subject to adiabatic processes; air that rises is subject to adiabatic expansion and is cooled, while the sinking air is subjected to adiabatic compression and is heated. The species involved in the airglow producing reactions - such as O, H and O₂ - have mixing ratios that vary greatly with height. A vertical displacement will produce a significant change in the concentration. It is worth noting that airglow observations are best suited to observation of waves with vertical wavelength $\lambda_z > 12km$. This is waves with wavelengths longer than the airglow layer. The horizontal wavelength should be confined within the field of view, i.e $\lambda_x < 300km$.

2.5 Mathematical Modelling of Gravity Waves

When modelling gravity waves in the atmosphere, the linear Boussinesq equations are good place to start.

$$\begin{aligned}
u_t - fv + \frac{1}{\rho_0} p'_x &= 0, \\
v_t + fu + \frac{1}{\rho_0} p'_y &= 0, \\
u_x + v_y + w_z &= 0, \\
-\frac{g}{\rho_0} \rho'_t + N_B^2 w &= 0, \\
p'_z + g\rho' &= 0,
\end{aligned} \tag{22}$$

In equation 22 ρ_0 is a reference density, g is the gravitational acceleration, N_B is the buoyancy frequency p with any index means pressure, f is the Coriolis-force term and u , v and w are velocities.

To simplify the modelling, plane wave solutions are sought for. By restricting this derivation to a comparatively small horizontal scale ($\lesssim 100km$), calculations are simplified as the rotation of the Earth has a negligible effect on this scale, i.e. the Coriolis terms can be neglected. This is the same as setting $f = 0$ in equation 22. In addition, N_B is said to be independent of z , an assumption that is fairly reasonable in both the troposphere and the stratosphere.

The plane-wave solutions should be on this form:

$$\{u, v, w, p', \rho'\} = Re\{\hat{u}, \hat{v}, \hat{w}, \hat{p}, \hat{\rho}\}e^{i(kx+mz-\omega t)} \tag{23}$$

In 22 the hatted sizes (\hat{u}) etc. are complex amplitudes. ω is the angular frequency. To obtain plane-wave solutions to the Boussinesq equation, 23 is substituted into 22 with the simplifications mentioned in the previous paragraph, resulting in the following equation:

$$\begin{aligned}
-i\omega\hat{u} + \frac{ik\hat{p}}{\rho_0} &= 0, \\
-i\omega\hat{v} &= 0, \\
ik\hat{u} + im\hat{w} &= 0, \\
\frac{i\omega g}{\rho_0} + N_B^2\hat{w} &= 0, \\
im\hat{p} + g\hat{\rho} &= 0,
\end{aligned} \tag{24}$$

Eliminating \hat{u} , \hat{v} , \hat{w} and $\hat{\rho}$ in favour of \hat{p} and arbitrarily choosing \hat{p} to be real, new equations emerge:

$$\begin{aligned}
p' &= \hat{p} \cos(kx + mx - \omega t), \\
u &= \frac{k\hat{p}}{\rho_0\omega} \cos(kx + mx - \omega t), \\
v &= 0, \\
w &= -\frac{k^2\hat{p}}{\rho_0\omega} \cos(kx + mx - \omega t), \\
\rho' &= \frac{m\hat{p}}{g} \sin(kx + mx - \omega t)
\end{aligned} \tag{25}$$

Equations 25 are known as the polarisation relations for the waves. The sizes u , w and p are phase-shifted 180 degrees with respect to each other, while ρ' is 90 degrees out of phase with each of them and $v = 0$. The polarisation relations must have a non-trivial solutions. This condition gives rise to the dispersion relation.

$$\omega^2 = \frac{N_B^2 k^2}{m^2} \tag{26}$$

This gives to possible solutions for the angular frequency:

$$\omega = \pm \frac{N_B k}{m} \tag{27}$$

Introducing the group velocity c_g to see how these two solutions represent quite different physics.

$$\begin{aligned}
c_g &= (c_g^{(x)}, 0, c_g^{(z)}) \\
&= \left(\frac{\delta\omega}{\delta k}, 0, \frac{\delta\omega}{\delta m} \right)
\end{aligned} \tag{28}$$

Of the components in 28, the z-direction component, i.e. the vertical component, is of particular interest.

$$c_g^{(z)} = \mp \frac{N_B k}{m^2} \tag{29}$$

By sticking to a convention of a positive k , and noting that for an upward propagating wave generated near the surface, the vertical component of the group velocity must be positive, i.e. $c_g^{(z)} > 0$. Therefore the convention of the minus sign in 28 is chosen.

$$\omega = -\frac{N_B k}{m} \tag{30}$$

As 30 demonstrates, a positive angular frequency leads to $m < 0$.

2.6 Filters

Narrowband interference filters allow for the isolation of wavelength intervals of a few nanometres or less, thus enabling the study of one transmission line without confusion from other lines. The sodium D-lines in the nightglow are located around 589 nm, separated by 0.6 nm. Interference filters are multi-layer thin film devices. Narrowband interference filters are mostly dielectric, but there are often metallic layers in auxiliary blocking structures. A common feature of interference filters is that transmittance and reflectance spectra will shift to shorter wavelengths as the filter is tilted away from normal incidence, see figure 7. Due to the angle of the incidence cone on the filters, the two lines from the sodium doublet will not be clearly defined, see figure 10.

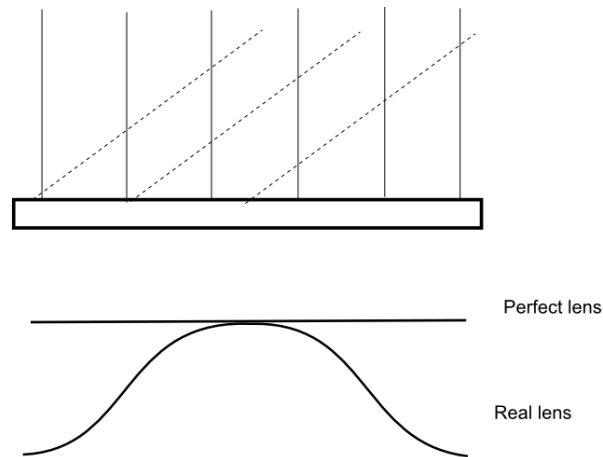


Figure 6: Transmittance through a real interference filter; the intensity falls off away when moving away from the centre.

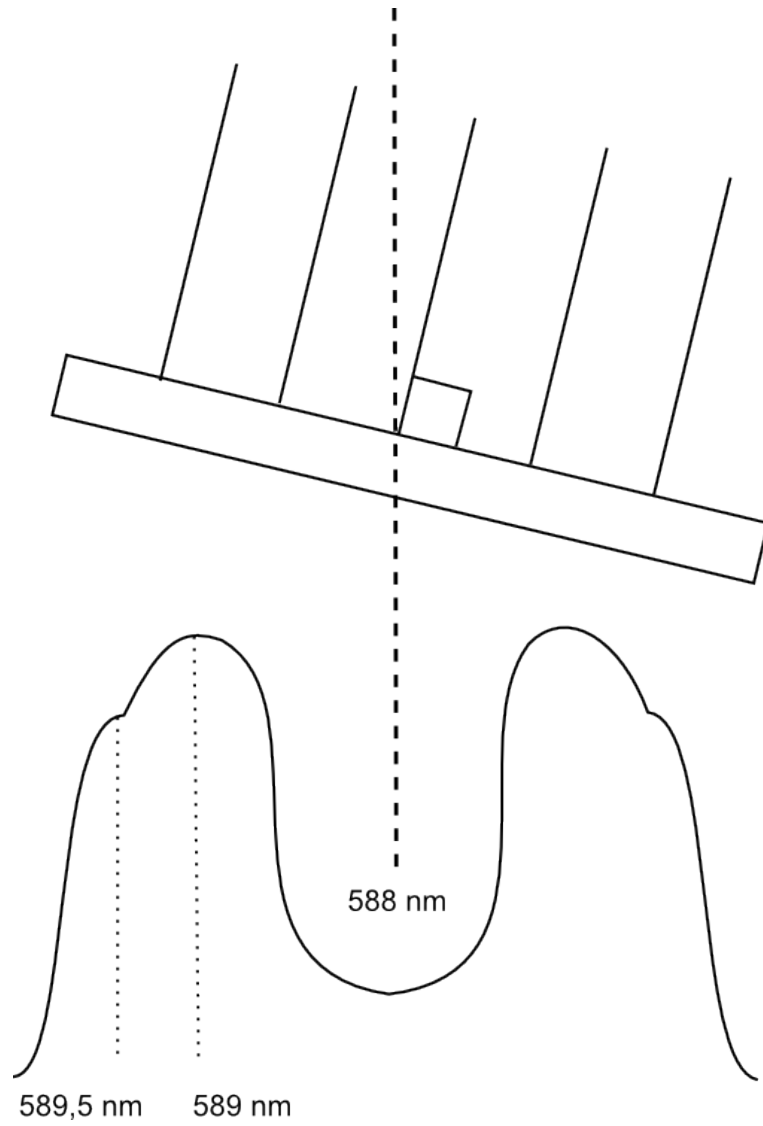


Figure 7: Transmittance of light from the sodium doublet when tilted away from normal incidence.



Figure 8: Light emitted from sodium lamp as seen through the broadband Na filter

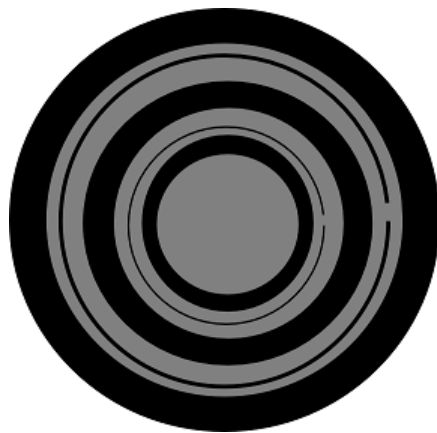


Figure 9: Light emitted from sodium lamp as seen through the narrowband Na filter

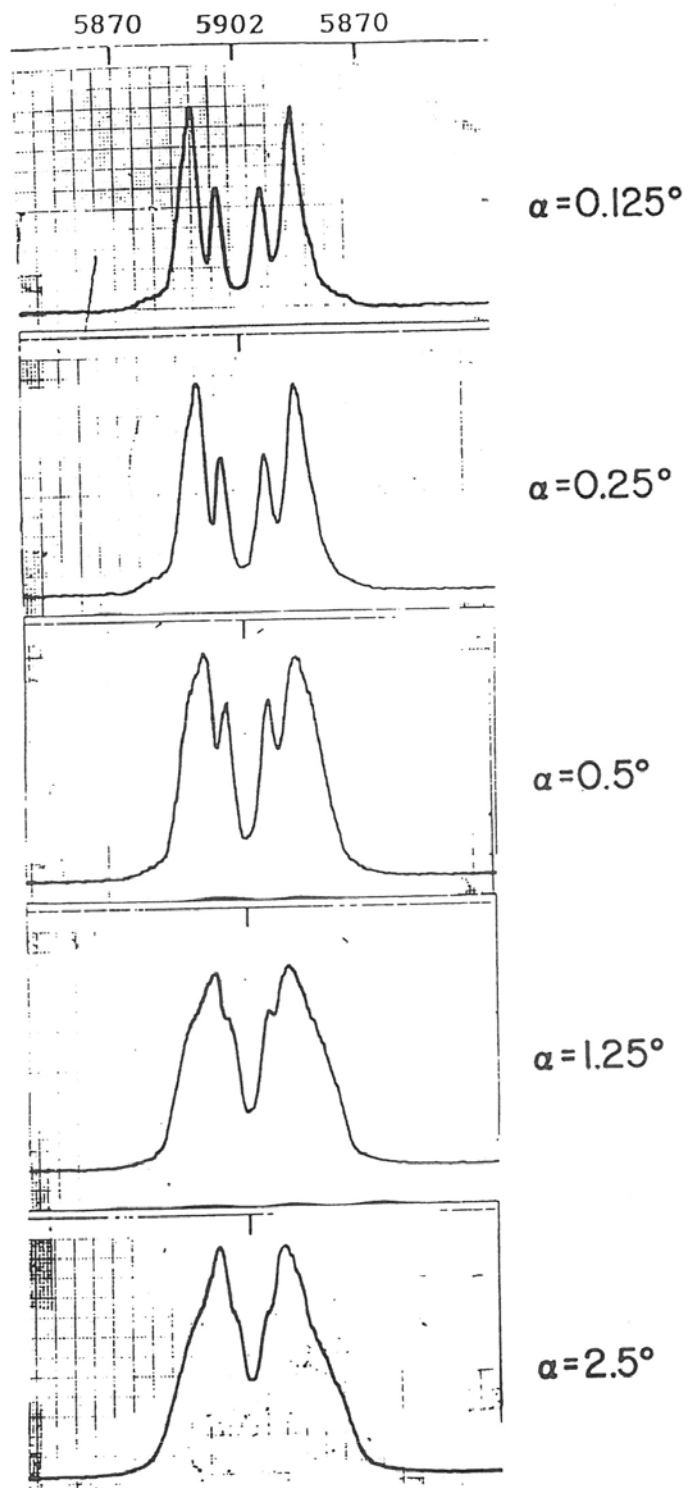


Figure 10: Broadening of the sodium doublet for 0.3 nm filter in a beam of half-cone angle α (normal incidence). The filter scans in wavelength from low to high and back again

3 Method

The primary focus of this project was to get a working imaging system to see whether variations in the sodium D-line ratio could be observed with the equipment. The equipment had already been in use at the University of Illinois, although primarily used for observing gravity waves using OH as a tracer instead of sodium.

The imaging system is placed at Dragvoll, imaging the night sky for solar evaluation angles of more than 14.7° degrees below horizon. This is within the interval of angles from 12° to 18° known as astronomical twilight. Astronomical twilight is generally accepted as the limit after which it is dark enough to take astronomical images of the night sky.

3.1 Imaging System

The imaging system consists of a telecentric lens system, a filter wheel, an optical extension tube and a CCD camera system.

3.1.1 CCD Camera

The camera is an Orion ParsecTM 8300M Monochrome Astronomical Imaging Camera. It has an 8.3 (8.5 effective) monochrome Kodak CCD chip sensor. It features benefits such as two-stage dual cooling and an internal shutter. The chip size of CCD is 5.4 micron x 5.4 micron pixel. The cooling system helps reduce noise and the internal shutter means that there is no need to cover the telescope at during the day to avoid damaging the CCD chip, and it also provides an easy way of controlling the exposure time.

3.1.2 Camera Control

The camera is controlled by the TakeIm.vbs file. This file controls the camera and the filter wheel, by opening the settings text file and assigning the exposure time and sequence from settings.txt to the MaxIm DL Pro, the camera software program. The task scheduler is responsible for the running of the TakeIm.vbs, which stops after a time given by the first line in settings.txt.

3.1.3 Optics of the Imaging System

A telecentric lens system has the advantage that the principal ray of all image-forming cones across the field of view cross the image plane parallel to the optical axis, making the maximum ray angles through the filter is determined by the F number of the lens.

Under low-light conditions such as airglow imaging, low F numbers are desirable. Lower F numbers mean higher ray angles through the filter, and so require filters of

wider bandwidth. However narrowband filters are readily available at much larger diameters than the imaging detectors, so that high F number images at the filter can be re-imaged to low F number images at the detector.

The front piece of the imaging system is a fish eye lens.

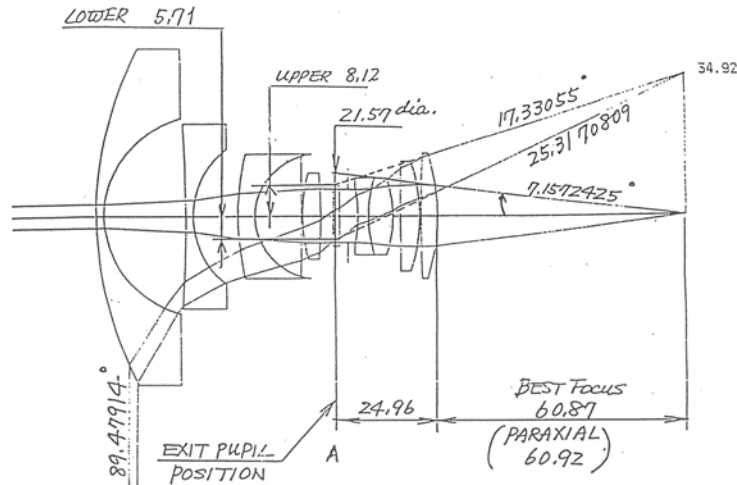


Figure 11: Ray diagram for a typical fish eye lens with F number of 4.0. The lens used at Dragvoll has a F number of 4.5.

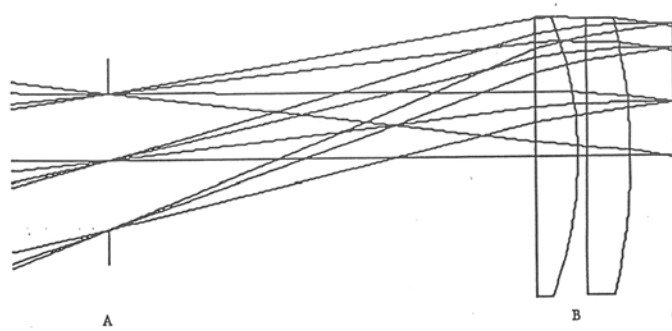


Figure 12: Right-hand part of the telecentric lens system with the addition of two plano-convex elements to produce a telecentric image

The effective focal length of the two plano-convex elements is chosen to equal the distance from the exit pupil of the lens to the principal plane of the two-lens combination. Thus the principal rays of the all image-forming cones are refracted parallel to the principal axis of the lens. This is what is known as the telecentric configuration; it allows

the use of narrowband interference filters whilst keeping the maximum ray angle through the filter dependent on the F number.

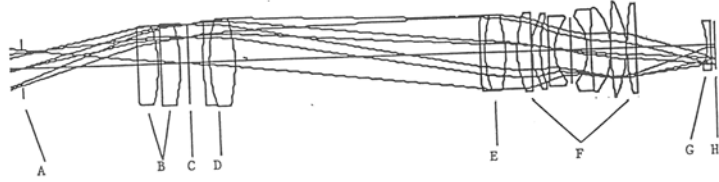


Figure 13: Optics of a typical re-imaging system

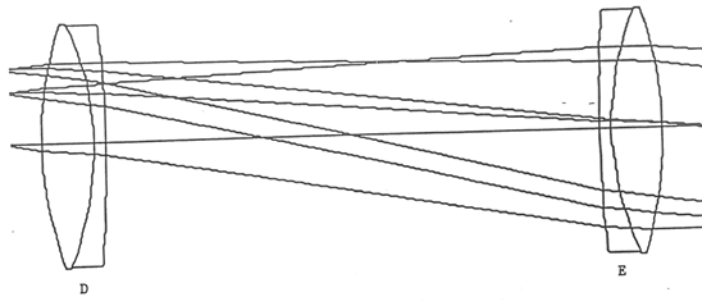


Figure 14: Field lens and close-up lens

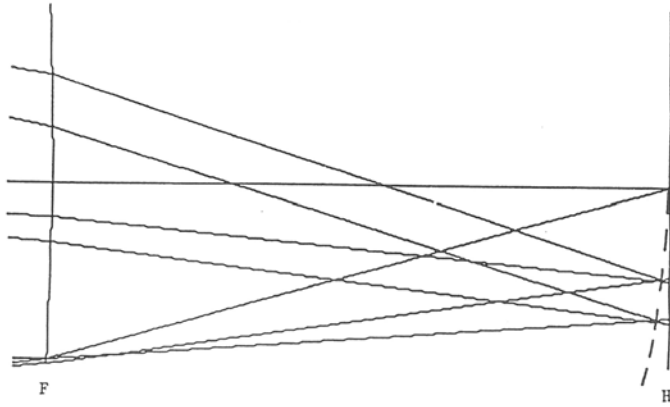


Figure 15: Field curvature without correction

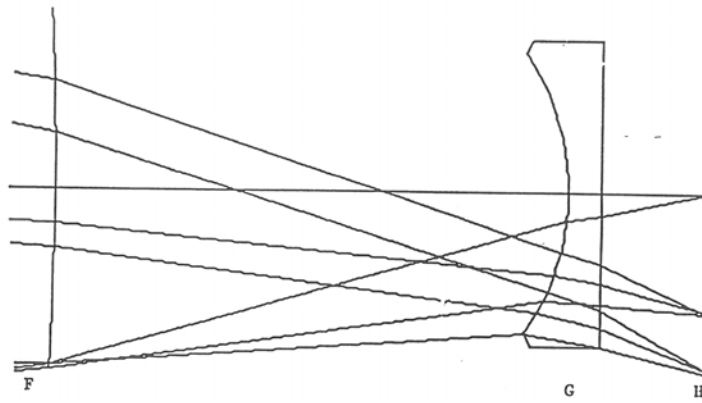


Figure 16: Field curvature with correction

3.2 The Filter Wheel

Inside the filter wheel, there are 5 filters, two of which are not currently at use at Dragvoll. The filter wheel rotates a filter to its designated position. Exposure time and exposure sequence is determined by the settings.txt file. Two of the filters are hydroxyl filters with distinctly different peak wavelengths, two filters are sodium filters centred around the same peak wavelength, but with different bandwidths. The last filter is a N_2^+ filter. The N_2^+ filter and one 885 nm OH filter are not currently being used for the imaging.¹

Table 1: Filter Position in the Filter Wheel

<i>Position</i> (-)	<i>Peakcentre/Bandwidth</i> (nm)	<i>Species</i> (-)
1	840/20	OH 6.2 band
2	590/3	Na
3	885/20	OH 7.3 band
4	590/0.3	Na
5	427/3	N_2^+

Initially, there was a $H\beta$ filter in place of the the narrowband sodium filter. However, the narrowband sodium filter has a much smaller diameter (52 mm) than the filter wheel dimensions which is designed to hold filters of 75 mm. To keep the narrow band sodium filter in place, a cardboard holder was made. The filter is kept in this holder by the help of some tape.

The focus of this project is to study the sodium D-line ratio. The hope is that the narrowband filter will be able to distinguish between the different lines in the spectrum from the night glow. Preliminary test were carried out in the lab to check if the filter could distinguish between the lines; the lines are only separated by 0.6 nm. A sodium lamp was brought into the lab. The lamp produces light that peaks at 590 nm, thus containing light from both the D_1 and D_2 line. The light is distinctly orange, much the same light as street lamps produce.

Looking at the sodium light through the filters, a bullseye pattern become apparent. However, though the narrowband filter a splitting of the rings can be seen. The same test was carried out by illuminating a reflectance screen and taking a picture of the screen with the imaging system. There were indications of splitting, but nothing definite could be said about it.

¹The ionised nitrogen line filter was re-included at December 7th.

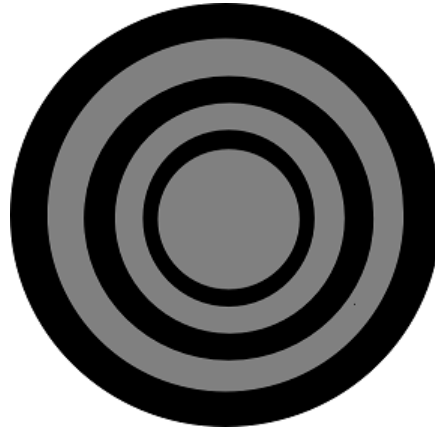


Figure 17: Light emitted from sodium lamp as seen through the broadband Na filter

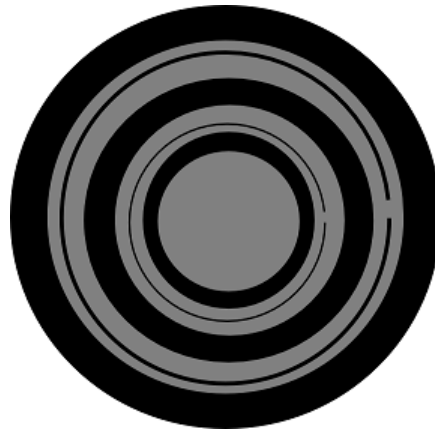


Figure 18: Light emitted from sodium lamp as seen through the narrowband Na filter

4 Results

As the O/O_2 ratio in the mesosphere is proportional to the concentration of hydroxyl, a spectral image of the hydroxyl will point to the optimal times at night to study the variations in the airglow. As it is necessary to add several of the narrowband images in order to obtain a signal to noise ratio capable of showing the structure, the shorter period waves cannot be used to study the D-line variations.

4.1 December 1st

Figure 19 shows a spectral image of hydroxyl variations in the MLT on December 1st. The blue line is from the 3,1 OH band and the red line is from the 4,2 OH band. The black line is sodium from the city light. If the black line rises as the red and blue lines

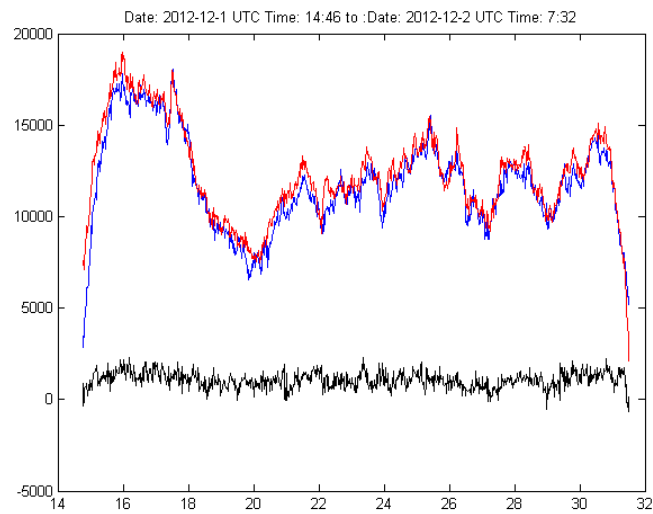


Figure 19: Spectral image of OH variations in the MLT on the 1st of December

drop it is indicative of a clouds coming into the field of view. On this night however, the data indicates that it was a clear night. All times are in UTC format.

For the images later in the night, the moon is coming up thus making the analysis of these images difficult.



Figure 20: Added image on December 1st

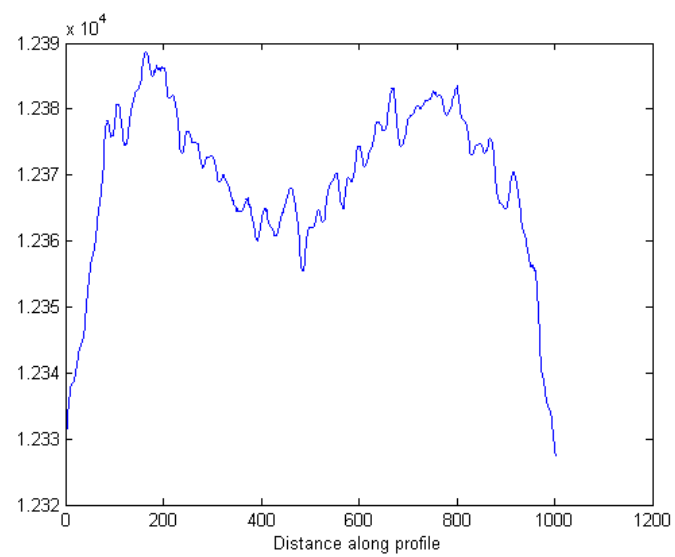


Figure 21: Intensity profile, 4 pictures added starting at 17:35.



Figure 22: Added image on December 1st, 4 images starting at 20:02

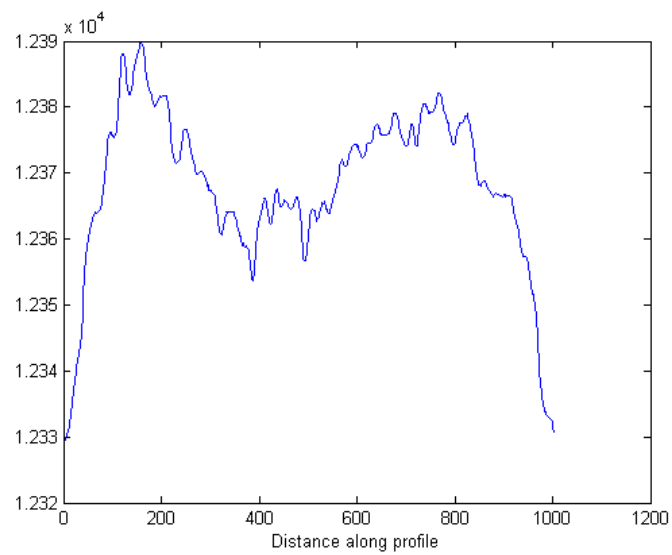


Figure 23: Intensity profile for 20:02 series.

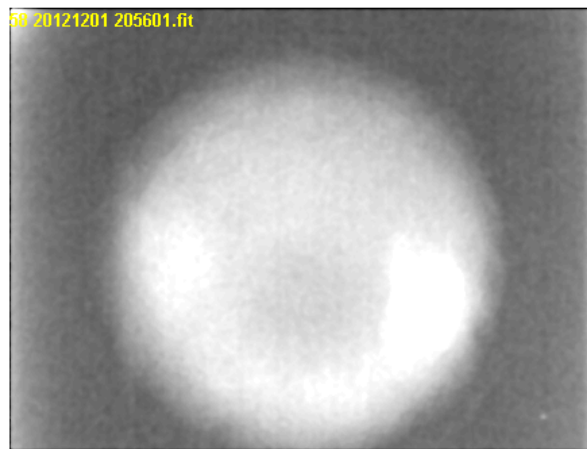


Figure 24: Added image on December 1st, 4 images starting at 20:56

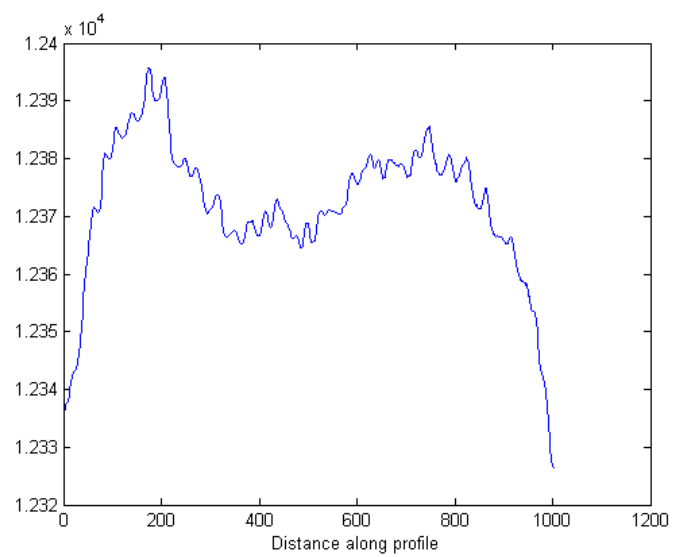


Figure 25: Intensity profile for 20:56 series.

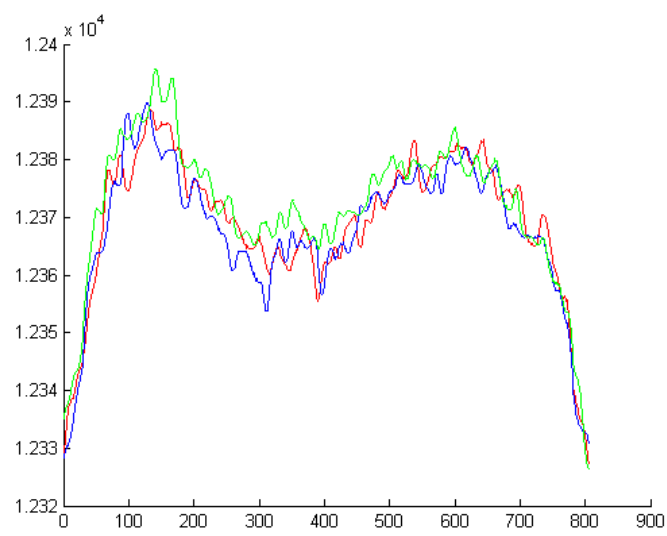


Figure 26: Intensity profiles in the same figure: red line is the 17:35 curve, blue line is the 20:02 curve and the green line is the 20:56 line.

4.2 December 3rd

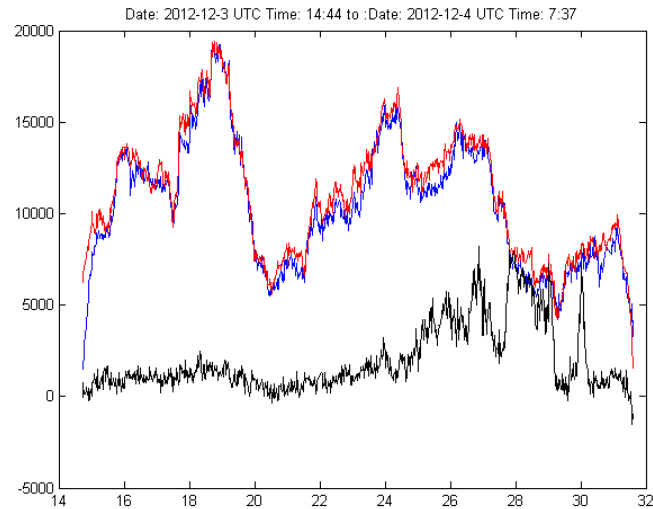


Figure 27: Spectral image of OH variations in the MLT on the 3rd of December

Figure 26 shows OH band intensities. The red line is from the 4,2 band, the blue line is from the 3,1 band. The black line is sodium from the city scattered from the cloud. When the layer of clouds is thick, much sodium is scattered off the clouds and OH is low due to absorption in the clouds. On the night of the 3rd to the 4th of December, there is a low sodium intensity until well after midnight. This indicates that this was a very clear night. Furthermore, there waves with long periods can from the minima and maxima; waves with periods on the scale of an hour or so.

It takes seven minutes to complete an image cycle. In other words, it takes seven minutes from the start of the exposure of one image in the narrowband filter to the start of the next exposure time in the narrowband. Four images added on top of each other therefore require a maxima/minima of roughly 28 min. Three images require 21 min. Consequently, broad peaks and valleys are of interest. From figure 26, such a broad peak can be found around 19:00. A broad valley is found around 21:00, and another broad peak is found around midnight.

Figure ?? is 4 images taken around 19:00 on the 3rd added and filtered. The ring structure is visible; a bright ring around a darker centre. An intensity profile is carried out in matlab across the same path for different times of the night when the hydroxyl concentration in the MLT is known to be different.

The figures 32 and 31 are not being studied in detail due to the 26 indicating the rise of a layer of clouds around this time of night.

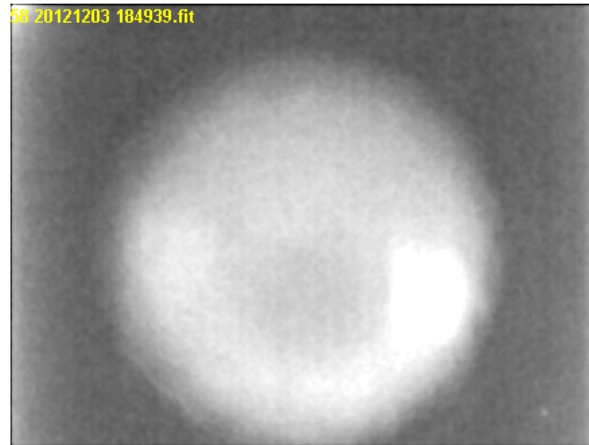


Figure 28: Added image around 18:49, 4 consecutive images

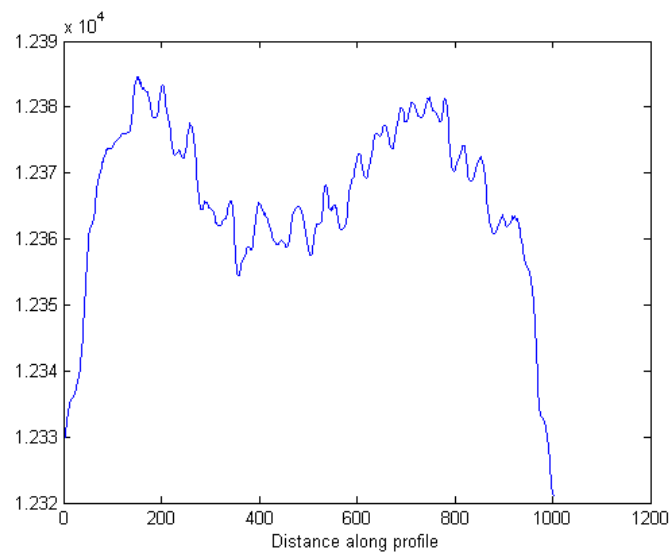


Figure 29: Profile at 18:49



Figure 30: Profile at 20:10

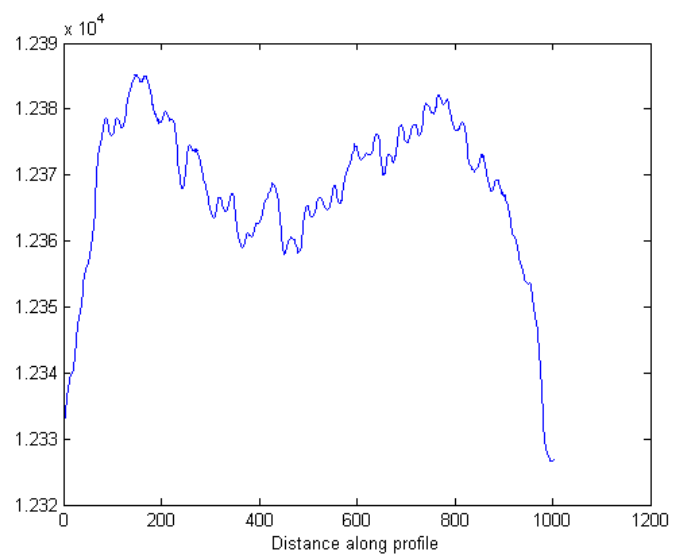


Figure 31: Profile at 20:10

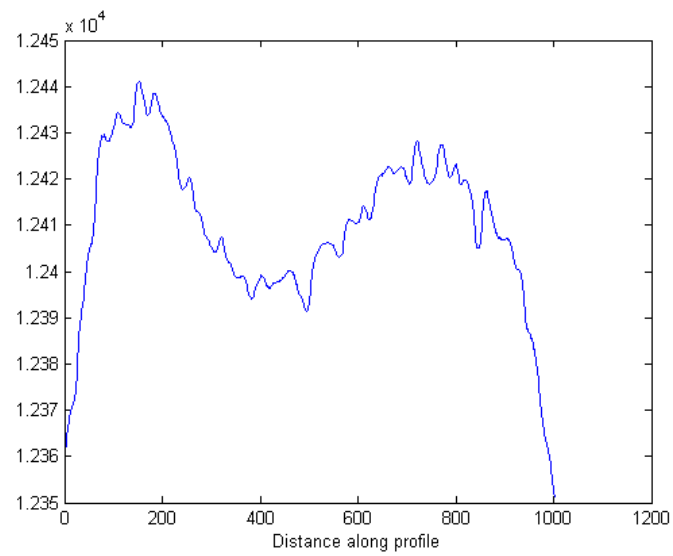


Figure 32: Profile at 23:54



Figure 33: Added image around 2354, 4 consecutive iamges

Plotting the the intensity plot 28 an 30 in the same figure makes for a good comparison between a high [OH] and a low [OH] period.

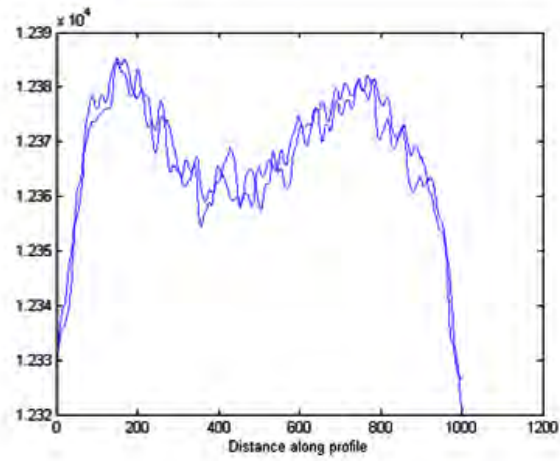


Figure 34: 18:49 and 20:10 intensity profiles in the same plot

For reference, plots of the nightglow in the broadband sodium filter are included.



Figure 35: Broadband sodium image around 1845

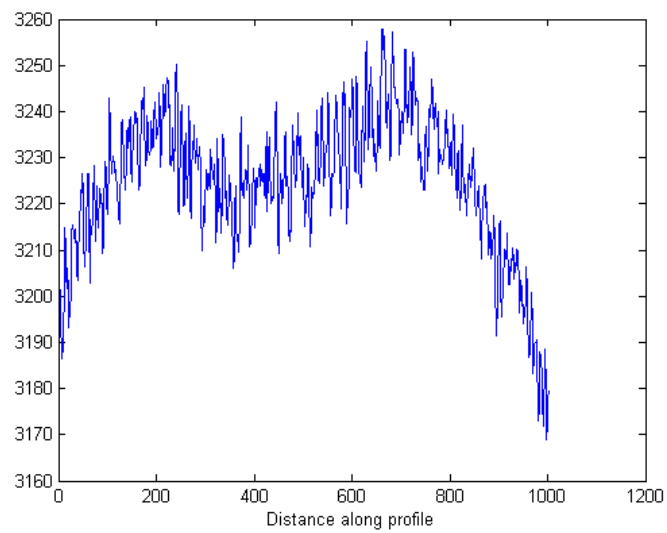


Figure 36: Intensity profile in the broadband sodium image around 1845



Figure 37: Broadband sodium image around 2014

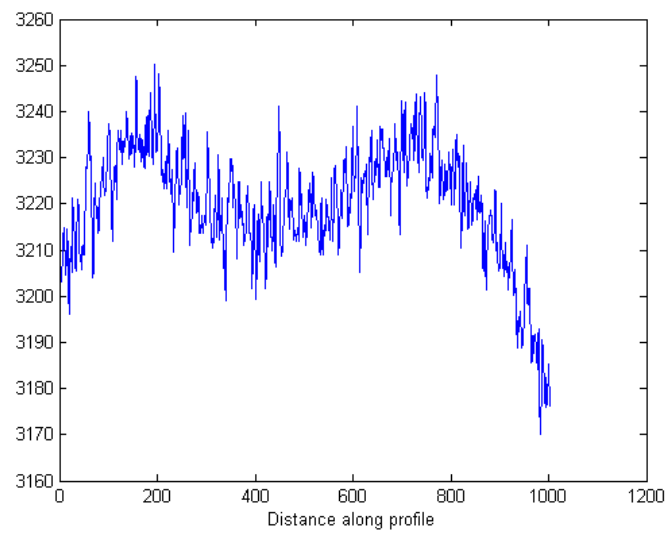


Figure 38: Intensity profile in the broadband sodium image around 2014

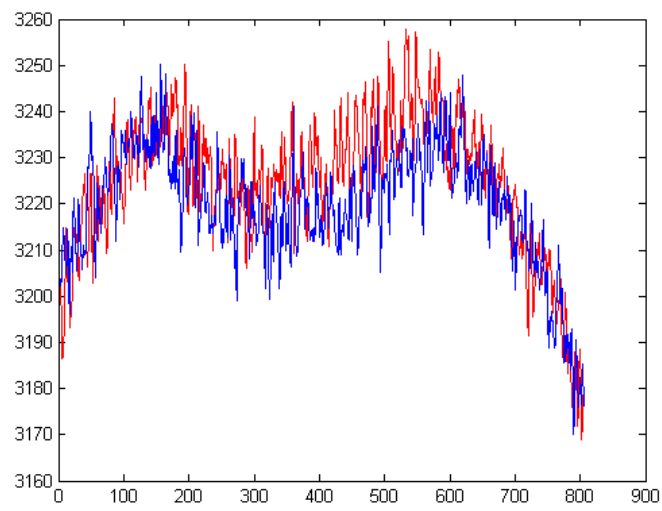


Figure 39: Intensity profile in the broadband sodium image, red curve is the 18:45 plot, blue curve is the 20:14 plot

5 Discussion

Due to the low bandwidth of the narrowband filter, it requires a long exposure time in order to obtain an acceptable signal to noise ratio. At first, the exposure time for this filter was set to 120 seconds, the same as the broadband sodium filter in order to acquire a even sequence of the hydroxyl images. At the 7. of December the exposure time was increased by 60 seconds and the N_2^+ filter was added to the sequence right after the broadband sodium to maintain the evenness of the hydroxyl imaging sequence important to another specialisation project.

In addition to increasing the exposure time, images are added together as a way to increase the signal to noise ratio. Four images are added to each other. The images are processed in matlab; each image is filtered with a two dimensional median filter, taking a 7 by 7 median, and then a 2 dimensional wiener filter and then again filtered with a 2 dimensional median filter with the 7 by 7 median. The same goes for the added images and the final image. The added images represent a rather long time period. Consequently, the gravity waves with the shorter wavelengths cannot be observed this way, and may in fact contribute to the noise in the images. However, data from the spectroscope help identify the hydroxyl variations in the MLT. These data show a wave structure with much larger time periods, as much as half an hour.

The narrowband filter, due to its smaller diameter was kept in place in a cardboard holder which was made to fit the dimensions of the filter wheel. The holder, while keeping the filter in place, tilts the filter slightly relative to normal incidence. A tilting of a transmission filter lead to a down-shifts of the central transmission wavelength. It also creates an asymmetry in the airglow images, as can be seen in the images where the dark spot in the middle is not centred in the middle of the airglow. This down-shift in central wavelength has the effect that the D_1 -line becomes more difficult to observe. Depending on the size of the tilt it may not even be possible to observe this line at all. However, as the D_1 increases the D_2 will decrease, and it should be possible to observe this decrease, by observing a broadening of the intensity curves.

5.1 Results

Figure 33 shows the intensity profile plot 28 and 30 in the same figure on the same axis. Figure 26 shows a decrease in hydroxyl intensity by a factor of 3. The intensity plots show no no sign of the D-line ratio being affected by this decrease in the hydroxyl intensity. Neither is there any significant change in the broadband intensity profiles, see figures 35 and 37. In the combined plot, 38, the red curve from 35 is slightly higher, but not as high as would be expected from an order of three higher hydroxyl intensity in that time period.

5.2 Problems Encountered in the Course of the Project

When dealing with a system beyond human control such as the atmosphere, many unforeseen phenomena may affect the results. Specifically, the success of this project depends primarily on gravity waves being present in the MLT and at having weather conditions that will allow for them to be observed. Since the weather conditions this autumn have not been optimal for observing gravity waves, the result material is somewhat meagre.

Besides, the lights from the city scatters off the lower clouds or even the air pollution. At first it was thought that the brighter spot at the bottom right of the images was caused by the lights from the city scattering off clouds or air pollution. However, as it is not present in the broadband filters the most likely cause is an anisotropy if the narrowband sodium filter.

The CCD camera may have been damaged on transport causing it to shut down or give out a blurry image for long periods of time on many nights. The Moon also causes problem; light reflected off the dome give trouble when analysing the intensity profile of the images. Initially, there was a problem with condensation on the dome obscuring the view. This was solved by installing a shoe-dryer on the wall and focusing the warm, dry air from the shoe-dryer into the area of the dome. This has also helped keep the dome clear of snow; only on night with very heavy snowfall has this not been sufficient to melt the snow. However as soon as the snowfall stops the the warm air causes it to melt.

6 Conclusion

There is no evidence of there being any change in the D-line ratio as the O/O_2 ratio changes. This could be due to the fact that the hydroxyl concentration is being used as a measure for the O/O_2 in the sodium layer when the hydroxyl layer peaks at 87 km and the sodium layer peaks at 90 km and there is the question of how fast the atomic oxygen is "used up" as it enters the MLT. It could be that the oxygen is completely used up in the lower part of the hydroxyl layer. However, due to the width of each layer, and the fact that they are only separated by 3 km this seems unlikely.